

Interplay between Mn-acceptor state and Dirac surface states in Mn-doped Bi₂Se₃ topological insulator

M. R. Mahani, A. Pertsova, M. Fhokrul Islam and C. M. Canali

Department of Physics and Electrical engineering, Linnaeus University, 391 82 Kalmar, Sweden

(Dated: May 29, 2021)

We investigate the properties of a single substitutional Mn impurity and its associated acceptor state on the (111) surface of Bi₂Se₃ topological insulator. Combining *ab initio* calculations with microscopic tight-binding modeling, we identify the effects of inversion-symmetry and time-reversal-symmetry breaking on the electronic states in the vicinity of the Dirac point. In agreement with experiments, we find evidence that the Mn ion is in the +2-valence state and introduces an acceptor in the bulk band gap. The Mn-acceptor has predominantly *p*-character, and is localized mainly around the Mn impurity and its nearest-neighbor Se atoms. Its electronic structure and spin-polarization are determined by the hybridization between the Mn *d*-levels and the *p*-levels of surrounding Se atoms, which is strongly affected by electronic correlations at the Mn site. The opening of the gap at the Dirac point depends crucially on the quasi-resonant coupling and the strong real-space overlap between the spin-chiral surface states and the mid-gap spin-polarized Mn-acceptor states.

PACS numbers: 73.20.Hb, 73.20.At, 71.15.-m,

I. INTRODUCTION

Topological insulators (TIs), characterized by a non-trivial insulating gap in the bulk and topologically protected helical states on the boundaries, are a new frontier in condensed matter physics and materials science^{1,2}. Topological surface states (TSSs) in three-dimensional (3D) TIs, such as the Bi₂Se₃ family with a single Dirac cone, have attracted particular attention³. While the TSSs are robust against time-reversal-invariant perturbations, the breaking of time-reversal symmetry (TRS) opens up an energy gap at the Dirac point. One way to explore the response of the TSSs to TRS breaking is via magnetic ordering. Apart from being a prerequisite for future spintronic applications, the presence of magnetic order in 3D TIs manifests itself in novel quantum phenomena, such as the quantum anomalous Hall effect^{4,5} and the topological magnetoelectric effect⁶.

A finite density of magnetic impurities on a 3D TI surface is expected to bring about a gapped magnetic phase, with magnetic moments coupled by a surface-state-mediated exchange interaction^{7,8}, similar to the carrier-mediated exchange coupling in dilute magnetic semiconductors (DMSs). However, before one can identify the nature of magnetic interactions, it is critical to understand the physics of individual magnetic dopants both in bulk and near the surface of a 3D TI. To date, there seems to be no consensus in experimental and theoretical literature on the behavior of different species of magnetic impurities in these systems. Contrasting results have been reported regarding the chemical trends and the magnetic state of the impurities⁹⁻¹², as well as the presence or absence of the energy gap at the Dirac point upon doping¹³⁻¹⁷. For instance, scanning tunneling spectroscopy (STM) and angular resolved photoemission spectroscopy (ARPES) experiments on Bi₂Se₃ family of 3D TIs have demonstrated the opening of the gap by doping with Fe

and Mn^{13,18-20}. However, more recent work reported striking robustness of the TSS in the presence of magnetic dopants, such as Fe, Co and Gd^{14-16,21}. Theoretical results also differ, with some density functional theory (DFT) calculations confirming the presence of the gap at the Dirac point²²⁻²⁵ and others suggesting different scenarios, including a shift at the Dirac cone from the center of the Brillouin zone,^{10,16} as well as strong dependence on the magnetization orientation and valence state across the transition-metal (TM) series¹¹.

We should also note that there exist other possible mechanisms for magnetic ordering in 3D TI systems, different from the carrier-mediated (RKKY) interaction^{7,26-28} typical of DMSs. It is known that in Bi₂Se₃ both the conduction and valence bands are formed by *p*-orbitals and that the spin-orbit interaction is strong, resulting in band inversion and an energy gap in the bulk. This leads to large matrix elements of the spin-operator between the wave functions of conduction and valence bands and, as a consequence, to a large Van Vleck spin susceptibility⁴. In contrast to DMSs, where this effect is usually small, in the Bi₂Se₃ family of 3D TIs this can lead to a ferromagnetic order even if the dopants do not introduce free carriers into the host material such as Fe dopants. Hence, possible mechanisms for magnetic interactions may vary depending on the nature of magnetic dopants and different dopant species must be carefully examined.

For the important case of magnetic acceptors, e.g. Mn on (111) Bi₂Se₃ surface, a detailed microscopic description, consistent with experimental observations, is lacking. There is a strong experimental evidence that Mn behaves as a substitutional acceptor in the Bi₂Se₃ family of 3D TIs^{19,29,30}. Typically, Mn substitutes Bi in Bi₂Se₃ in the (*d*⁵) configuration, corresponding to the +2 valence state, giving rise to a spin $S = 5/2$. Since the nominal valence of Bi is +3, this implies that substitutional Mn impurities also introduce acceptor (hole) states

in the bulk gap of the host material, similarly to Mn in GaAs, a typical DMS. These acceptor levels can be directly probed by STM¹⁹. However, the nature of these states and their interplay with the Dirac surface states have not yet been analyzed theoretically.

In this work we investigate single substitutional Mn impurities on the (111) surface of Bi₂Se₃, using DFT and tight-binding (TB) models. We find that Mn⁺² introduces a mid-gap acceptor state, localized mainly on the impurity and the nearest-neighbor (NN) Se atoms, similar to a substitutional Mn in GaAs³¹. Our calculations demonstrate the importance of electronic correlations at the impurity site, which we model by a Hubbard U parameter³². The U parameter controls the position of the impurity d -orbitals, which in turn determines the hybridization with the p -orbitals of NN Se atoms and the acceptor spin-polarization. Increasing U localizes the Mn d -states, leading to an enhancement in the Mn magnetic moment and a weakening of the p - d hybridization and the acceptor polarization. With the Mn placed on one of the surfaces of a finite slab, the spin-polarized acceptor states couple quasi-resonantly with the helical TSS at the same surface, opening a gap of a few meV at the Dirac point. The magnitude of the gap is significantly affected by the strength of the p - d hybridization. With the appearance of the energy gap, the system exhibits a finite out-of-plane magnetization^{7,8}.

The rest of the paper is organized as follows. In Section II we discuss the details of the DFT calculations and the TB model for magnetic and nonmagnetic impurities in Bi₂Se₃. The results of DFT and TB calculations are presented in Section III. In particular, we describe modifications in the electronic bandstructure of a Bi₂Se₃ slab, induced by doping, and analyze the electronic and spin properties of the acceptor states, associated with Mn impurities. The role of the spin-polarized acceptor states in the opening of the gap at the Dirac point is discussed. Finally, we draw some conclusions.

II. COMPUTATIONAL MODELS

The DFT calculations were performed using the full-potential all-electron linearized augmented plane waves method as implemented in the WIEN2k package³³. The generalized gradient approximation (GGA) is used for exchange correlation functional³⁴. We consider a 2×2 surface supercell containing six quintuple layers (QLs) of Bi₂Se₃. A Bi atom in the topmost Bi monolayer (ML) is replaced by a Mn (Mn doping of 2%). The direction of the magnetization is along [001] (z -axis), which is perpendicular to the (111) surface. A vacuum of 30 Bohr is added along the [001] direction to avoid supercell interaction. The atomic positions in the supercell have been fully relaxed. We use four non-equivalent k -points in the Brillouin zone. Electronic correlations at the impurity site are accounted for by means of the (GGA+ U)-method. In Section III we will consider

explicitly the two cases $U = 0$ and $U = 4$ eV³¹.

In addition to DFT calculations, to model the electronic structure of pristine Bi₂Se₃, we use the sp^3 Slater-Koster TB Hamiltonian with parameters fitted to DFT calculations, which has been discussed extensively in Ref. 35 and 36. An impurity is introduced in the TB Hamiltonian via a local modification of the on-site potential at the impurity site. For a non-magnetic impurity, the on-site energy is modified as $\tilde{\varepsilon}_{i\alpha\sigma} = \varepsilon_{i\alpha} + \varepsilon_{i\alpha}^p$, where i is the index of the atom where impurity is located, α is the orbital index and σ is the spin; $\varepsilon_{i\alpha}$ is the spin-independent on-site energy of atom i in the pristine case and $\varepsilon_{i\alpha}^p$ is a spin-independent potential shift. For numerical calculations we choose a value $\varepsilon_{i\alpha}^p = 0.75 \varepsilon_{i\alpha}$, which generates a shift between the TSSs, corresponding to top and bottom surfaces, of the same order of magnitude as that obtained in our DFT calculations. In the case of a magnetic impurity, we assume that, apart from an overall potential shift, the impurity induces a local spin-splitting. Therefore the modified on-site energy of the impurity atom is written as $\tilde{\varepsilon}_{i\alpha\sigma} = \varepsilon_{i\alpha} + \varepsilon_{i\alpha}^p \pm \varepsilon_{i\alpha}^s$ (+ for $\sigma = \uparrow$ and - for $\sigma = \downarrow$; the spin-quantization axis is along the z -axis, perpendicular to the (111) surface of a Bi₂Se₃ slab). The spin-dependent part of the on-site potential, $\pm \varepsilon_{i\alpha}^s$, which is taken to be a fraction of $\varepsilon_{i\alpha}$, enforces a net out-of-plane magnetization and generates a small gap at the Dirac point of the TSS of the doped surface (top in our calculations). This crude impurity model allows us to illustrate the main features of the electronic bandstructure, associated with inversion symmetry (IS) and TRS breaking.

III. RESULTS AND DISCUSSIONS

We start with the DFT bandstructure of a pristine Bi₂Se₃ slab, plotted in Figs. 1(a)-(b), showing the expected conical TSS crossing at the Dirac point. The TSS consists of two degenerate states, one for each slab surface. For the particular slab considered, these states are only slightly coupled, introducing a small ($\lesssim 1$ meV) gap at the Dirac point.

The DFT bandstructure of Mn dopants substituted on one (the TOP) of the slab surfaces is plotted in Fig. 1(c), for the case $U = 0$. It is characterized by the following features: (i) the conical TSS belonging to the top surface (where the impurity resides) has been pushed up in energy. The bottom TSS is essentially unaffected by the impurity [see also Figs. 1(d)-(e), where the bottom and top states are highlighted]; (ii) the two displaced conical TSSs exhibit avoided level crossings, with a gap of the order of 20 meV, at two symmetric k -points with respect to Γ ; (iii) the Dirac point of the top (bottom) TSS is now above (below) the Fermi energy ($E = 0$). For the top TSS there is an energy gap of ≈ 5.5 meV at the Dirac point [see the inset in Fig. 1(c)]. As we explain below, this gap is caused by the TRS breaking due to

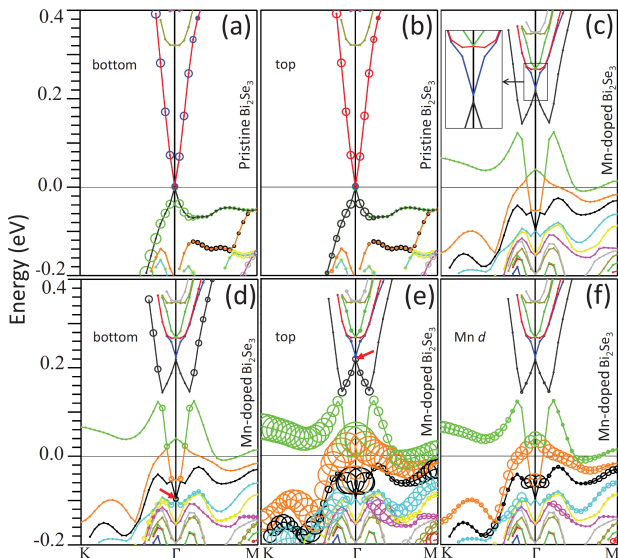


FIG. 1. Bandstructure of pristine (a,b) and Mn-doped (c-f) Bi_2Se_3 , calculated with DFT for $U=0$. Inset shows the gap at the Dirac point caused by the TRS breaking. Circles show the contribution of the bottom (a,d) and top (b,e) surface states, and of the Mn d -orbitals (f). The radius of the circles is proportional to the relative weight at a given energy and k -point. Arrows in panels (d) and (e) mark the Dirac points of the bottom and top TSS, respectively.

magnetic doping. For the bottom TSS the gap remains negligible, i.e. ~ 1 meV, as in the pristine case; (iv) the states in the energy window $E \in [0, 0.13]$ eV, not belonging to the bottom TSS, result from the complex hybridization of Mn d -levels, NN Se p -levels and the extended top TSS.

The ≈ 5.5 meV gap at the Dirac point obtained in our calculations matches reasonably well the ≈ 7 meV gap found experimentally for 1% Mn doping in Bi_2Se_3 ¹³. The energy gap is expected to increase for higher doping concentrations.

In order to explain some of these features, we employ the sp^3 TB model for Bi_2Se_3 , described in Section II. Figures 2(a)-(b) show the bandstructure of 6QLs of Bi_2Se_3 calculated with the TB model, where a non-magnetic or a magnetic impurity is substituting Bi in the second ML below the surface. In the non-magnetic case, as a result of asymmetric doping, one of the two degenerate (for pristine Bi_2Se_3) conical TSSs, corresponding to the doped surface, is shifted up in energy. The TSS of the un-doped surface remain nearly unaffected, as expected for a relatively thick slab. Since the TRS is preserved, the states at Γ have a two-fold degeneracy related to the opposite spins [top inset in Fig. 2(a)]. However, the asymmetric doping breaks the inversion symmetry (IS), therefore away from Γ the degeneracy is lifted and avoided crossings are formed at two symmetric k -points, producing a gap, which can be seen in the middle insets in Figs. 2(a) and (b) (this gap should vanish in the limit of an infinitely thick slab). The presence of

the magnetization breaks the TRS, which leads to the lifting of the degeneracy at all k -points. Indeed, in the magnetic case, in addition to the features related to asymmetric doping, we find a gap at the Dirac point (Γ) for the TSS of the doped surface [top inset in Fig. 2(b)]. We focus specifically on three important regions in the bandstructure, namely the Dirac point of the top surface states (unperturbed) [top inset in Fig. 2(b)], which interact with impurity, the Dirac point of the bottom surface states (unperturbed) [bottom inset in Fig. 2(b)], and the avoided level crossings, which occur symmetrically on both sides of the Γ point and introduce a small gap [middle inset in Fig. 2(b)]. The latter feature, as well as the overall shape of the bandstructure consisting of two shifted Dirac cones, is present in both non-magnetic and magnetic cases. As we explain in detail below, it is caused purely by IS breaking since the impurity is positioned on only one of the surfaces of the slab. However, the crucial difference between non-magnetic and magnetic impurities is the opening of the gap at the Dirac point of the TSS of the top surface, where the impurity is located. This is a manifestation of the TRS breaking. Note that the bottom TSS remain essentially unperturbed by the impurity in both cases.

We further investigate the effect of asymmetric doping by placing a non-magnetic impurity at different positions in the slab [see Fig. 2(c)-(e)]. Note that in this case the impurity substitutes Se and we use a 5QL slab; such configuration allows us to position the impurity at the exact geometrical center of the slab, which is a Se monolayer (ML). We use a similar potential shift, $\varepsilon_{i\alpha}^p = 0.75 \varepsilon_{i\alpha\sigma}$, as in the case of impurity substituting Bi. Placing the impurity close to one of the surfaces shifts the corresponding Dirac cone while the other one remains unchanged, provided that the slab is thick enough so that the two surfaces do not interact strongly with each other [Fig. 2(c)]. As the impurity is moved further away from the surface, its interaction with the topological surface states on the corresponding surface decreases, reducing the shift of the Dirac-cone states [Fig. 2(d)]. Finally, when the impurity is placed in the middle of the slab, the IS is restored and we find two degenerate Dirac cones with the position of the Dirac point coinciding with that of the pristine slab. Based on these calculations, we attribute similar features occurring in the vicinity of the Fermi energy in the DFT bandstructure [See Fig. 1(c)] to the IS breaking caused by asymmetric doping.

We now focus on the properties of the unoccupied electronic states, appearing above the Fermi level in our DFT bandstructure calculations [Figs. 1(c)-(f)]. There are three elements contributing to these states, (i) the impurity levels (Mn d -orbitals), (ii) the Mn-acceptor states, and (iii) the TSSs. Figure 3 shows the spin-resolved density of states (DOS) around the Fermi energy for the p -orbitals of Se atoms on the top and bottom surfaces and for the Mn d -orbitals, for $U=0$ and $U=4$ eV.

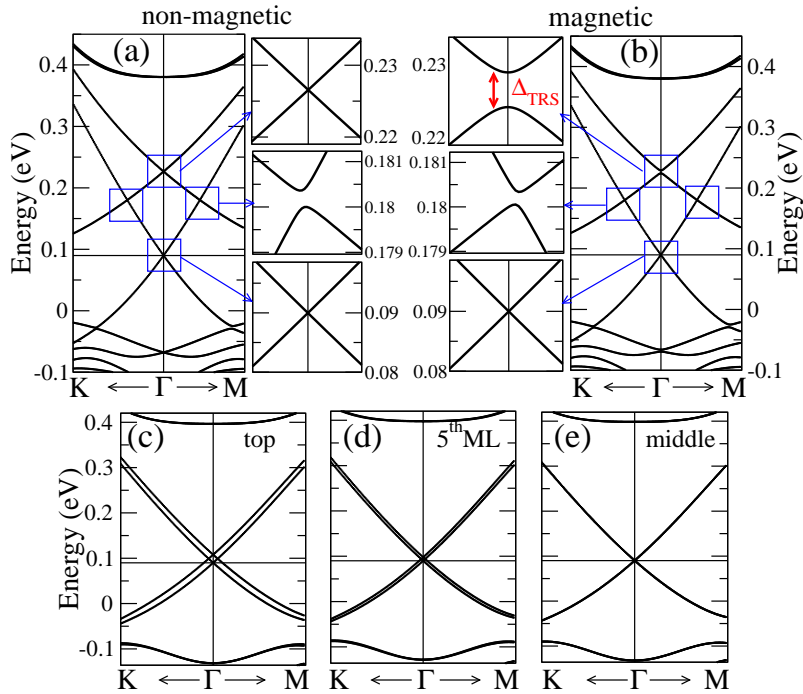


FIG. 2. (Color online) Bandstructure of Bi₂Se₃ calculated with the TB model using a 3×3×6QL supercell with (a) a non-magnetic and (b) a magnetic impurity, substituting a Bi atom in the topmost Bi ML. Bandstructure for a non-magnetic impurity at different depth in a 3×3×5QL slab: (c) topmost ML, (d) 5th ML below the surface and (e) 13th ML, corresponding to the middle of the slab.

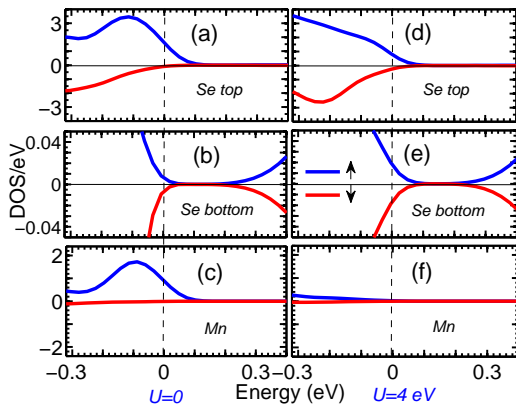


FIG. 3. Partial p -DOS for Se atoms in the top two (a,d) and bottom two (b,e) Se MLs; (c,f) d -DOS for the Mn impurity. Left panels are for $U=0$, right panels for $U=4$ eV. Positive (negative) DOS corresponds to majority (minority) spin. The vertical line marks the position of the Fermi level ($E = 0$).

The calculated magnetic moment of the Mn atom on the surface, with spin orbit interaction (SOI), is $4.67 \mu_B$ for $U=4$ eV, indicating that a substitutional Mn is close to its +2 valence state. Given the nominal +3 valence state of Bi in Bi₂Se₃, we conclude that the substitution of a Bi with a Mn introduces an acceptor (hole) state. Its wave function is localized primarily on the surroundings of the dopant and, to a lesser

degree, on the dopant itself. For $U=0$ some of the Mn d -orbitals appear close to the Fermi level [Fig. 3(c)], in the same energy range as the Se p -orbitals, leading to their hybridization. Importantly, the top surface Se p -states around the Fermi level are visibly spin-polarized [Fig. 3(a)]. The d -hybridized Se p -orbitals above the Fermi level close to the Mn are the main contributors to the Mn-acceptor (hole) states. With increasing U , the majority Mn d -orbitals are pushed deeper into the valence band [Fig. 3(f)], decreasing the hybridization with Se p -orbitals on the top surface. As a result, the Mn magnetic moment increases by $\sim 7\%$ with respect to the $U = 0$ value and the spin-polarization of the top Se p -states decreases [Fig. 3(d)]. We find a similar dependence of the magnetic moment on electronic correlations for Mn in the bulk, namely, $4.25 \mu_B$ for $U=0$ and $4.52 \mu_B$ for $U=4$ eV. These results suggest that the discrepancy between recent DFT calculations, reporting the values for the Mn magnetic moment ranging from $4 \mu_B$ ^{9,11} to $4.58 \mu_B$ ^{10,24} for Bi₂Se₃ and Bi₂Te₃, might be originating from different treatment of electron interactions on the impurity site.

The appearance of these unoccupied states above the Fermi level, spatially localized around the Mn, is an indication of the acceptor level. These states occur in the same energy range $E \in [0, 0.13]$ eV of the TSS of the top surface, and energetically are not far from its Dirac point. This is crucial for the opening of the gap. In contrast, in the range $E \in [0, 0.13]$ eV, the bottom

surface states [Figs. 3(b) and (e)] are essentially the TSS, with negligible coupling to the impurity wavefunction. Their linear dispersion is preserved and still detectable in the bandstructure in Fig. 1(d).

To clarify the nature of the Mn-acceptor independently of the TSS, we perform calculations without SOI, which greatly simplifies the electronic structure around the Fermi energy. Figures 4(b)-(e) show the total DOS and

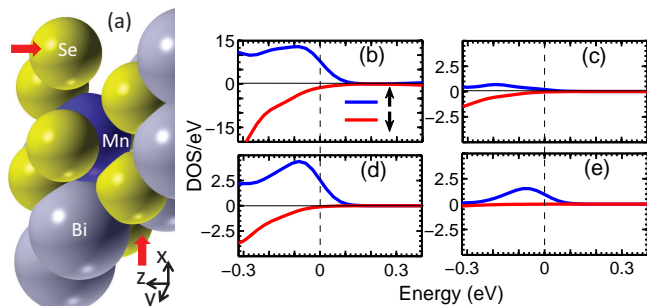


FIG. 4. (a) (111) Bi₂Se₃ surface with a Mn impurity in the second ML. DOS around the Fermi energy for Mn-doped Bi₂Se₃ slab for $U=0$ without SOI: (b) total DOS, (c) partial p -DOS for the two Se atoms above and below Mn, which are *not* NN to Mn [indicated by arrows in panel (a)], (d) partial p -DOS for the six NN Se atoms, (e) partial d -DOS for the Mn impurity. Note that the total DOS in panel (b) includes contributions from all atoms in the supercell and from the interstitial region.

the partial DOS for the Mn impurity and surrounding Se atoms, calculated without SOI. We conclude that the peak in the total DOS (mainly majority spin) right below the Fermi level, is predominantly due to the Mn d -levels and the NN Se p -levels, with a very small but finite contribution from other Se atoms around the Mn [two Se atoms, which are not NN to Mn, are indicated by arrows in Fig. 4(a)]. The highly spin-polarized character of the p -states around the Fermi level is a consequence of the hybridization between the Mn d -orbitals and the NN Se p -orbitals. Our calculations with $U=4$ eV (not shown here) confirm this observation. Similar to the calculation with SOI (see Fig. 3), for $U=4$ eV the Mn d -orbitals are more localized and are pushed deeper into the valence band, which reduces the p - d hybridization and decreases the polarization of NN Se p -states by a factor of two.

We now examine the spatial character of the Mn acceptor state, which is directly accessible by STM experiments. Figures 5(b)-(e) show simulated STM topographies of Mn-doped Bi₂Se₃ in the vicinity of the (111) surface. These images are obtained by plotting the electronic local density of states (LDOS) around the Mn, integrated in the energy window $[0, 0.13]$ eV (empty states) and $[-0.13, 0]$ eV (filled states) around the Fermi level for $U=0$. Figures 5(c) and (e) clearly show that the acceptor state is predominately localized around the Mn and its three NN Se atoms. The state is composed of three p -like Se orbitals pointing to the Mn

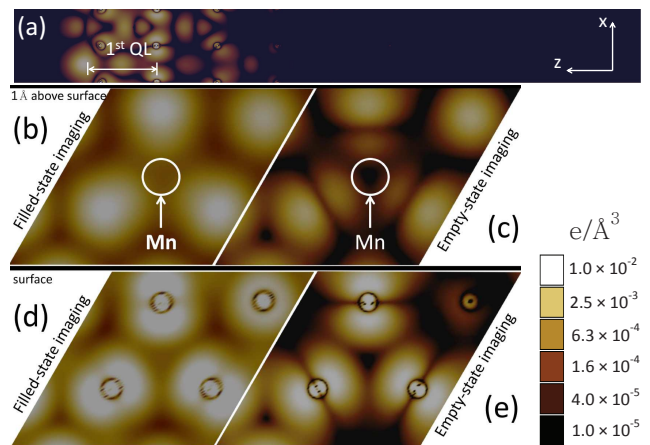


FIG. 5. LDOS of Mn-doped Bi₂Se₃ integrated over the energy range ± 0.13 eV around the Fermi level. Positive (negative) energy window correspond to empty-(filled-)state imaging. (a) Empty-state LDOS projected in the xz -plane, perpendicular to the (111) surface. LDOS projected on the the (111) surface: (b,c) at 1 Å above and (d,e) exactly on the surface. Left (right) panels are for filled (empty) states. Note the logarithmic color-scale.

in the middle, visibly deformed by the hybridization. It exhibits a characteristic triangular shape similar to the experimental STM topography observed at positive bias in Mn-doped Bi₂Te₃¹⁹. The LDOS for filled states below the Fermi level [Figs. 5(b) and (d)] are much less affected by the presence of the impurity.

The side view of the empty-state LDOS along the slab [Fig. 5(a)] confirms that the states in the energy range $[0, 0.13]$ eV are predominantly localized around Mn and its NN Se atoms, which is a signature of the Mn-acceptor. The figure also shows states that extend only within ~ 1 QL from the surface, which is a typical decay length of the TSS³⁶. Clearly, the Mn-acceptor has a strong spatial overlap with the TSS of the top surface. Furthermore, as shown above, these two states are quasi-degenerate in the energy range $[0, 0.13]$ eV, and therefore they couple strongly. It is precisely the quasi-resonant coupling of the spin-chiral TSS with the spin-polarized Mn-acceptor that ultimately opens a gap at the Dirac point. Strong support for this mechanism is provided by the observation that the gap decreases from 5.5 meV to 3.2 meV when U increases from 0 to 4 eV. Strong correlations at the impurity site decrease the Mn d - and Se p -orbital hybridization, leading to a smaller spin-polarization of the acceptor. Isolated spin-polarized Mn d -levels are further away both in energy and in space from the TSS at the Dirac point. Therefore their spin-dependent potential alone is less effective in inducing the TRS breaking necessary to open a gap.

IV. CONCLUSIONS

In conclusion, our calculations show, in agreement with experiments^{19,29,30}, that substitutional Mn impurities on Bi₂Se₃ surface introduce spin-polarized acceptor states, whose properties are similar to Mn-acceptors in GaAs. The mechanism for the opening of a gap at the Dirac point is provided by the spatial overlap and the quasi-resonant coupling between the Mn-acceptor and the TSS inside the bulk band gap of Bi₂Se₃. The signatures of this coupling can be detected in STM experiments, addressing specifically magnetic dopants on a 3D TI surface. The present study contributes to clarify the origin of surface-ferromagnetism in transition-metal-doped Bi-chalcogenide thin films.

Finally, we should mention that recent infrared optical experiments in Mn-doped Bi₂Te₃ thin films suggest that, despite the similarities to DMSs, carrier-independent mechanisms such as super-exchange⁹ and the aforementioned enhanced Van Vleck spin susceptibility⁴, might also be relevant for establishing the ferromagnetic state³⁷. Specifically these experiments indicate that bulk charge carriers control the optical response but do not seem to play a significant role in mediating

ferromagnetism. Note, however, that Mn-doped systems investigated in Ref. 37 are always n-type rather than the expected p-type for substitutional Mn, with the Fermi energy always located in the Bi₂Te₃ conduction band. The reason of this fact is still unclear. In any case these systems are in a regime quite different from the one studied in the present paper, where the position of Fermi energy is characteristic of a p-type DMS. Further experimental and theoretical studies, addressing the role of bulk dopants and the position of the Fermi level in the bulk band gap, are necessary to elucidate this point.

ACKNOWLEDGMENTS

This work was supported by the Faculty of Technology at Linnaeus University, by the Swedish Research Council under Grant Number: 621-2010-3761, and the Nord-Forsk research network 080134 “Nanospintronics: theory and simulations”. Computational resources have been provided by the Lunarc center for scientific and technical computing at Lund University.

-
- ¹ M. Z. Hasan and C. L. Kane, *Rev. Mod. Phys.* **82**, 3045 (2010).
- ² X.-L. Qi and S.-C. Zhang, *Rev. Mod. Phys.* **83**, 1057 (2011).
- ³ H. Zhang, C.-X. Liu, X.-L. Qi, X. Dai, Z. Fang, and S.-C. Zhang, *Nature Physics* **5**, 438 (2009).
- ⁴ R. Yu, W. Zhang, H.-J. Zhang, S.-C. Zhang, X. Dai, and Z. Fang, *Science* **329**, 61 (2010).
- ⁵ C.-Z. Chang, J. Zhang, X. Feng, J. Shen, Z. Zhang, M. Guo, K. Li, Y. Ou, P. Wei, L.-L. Wang, Z.-Q. Ji, Y. Feng, S. Ji, X. Chen, J. Jia, X. Dai, Z. Fang, S.-C. Zhang, K. He, Y. Wang, L. Lu, X.-C. Ma, and Q.-K. Xue, *Science* **340**, 167 (2013).
- ⁶ X.-L. Qi, T. L. Hughes, and S.-C. Zhang, *Phys. Rev. B* **78**, 195424 (2008).
- ⁷ Q. Liu, C.-X. Liu, C. Xu, X.-L. Qi, and S.-C. Zhang, *Phys. Rev. Lett.* **102**, 156603 (2009).
- ⁸ J. G. Checkelsky, J. Ye, Y. Onose, and Y. Tokura, *Nature Physics* **8**, 729 (2012).
- ⁹ C. Niu, Y. Dai, M. Guo, W. Wei, Y. Ma, and B. Huang, *Appl. Phys. Lett.* **98**, 252502 (2011).
- ¹⁰ J. Henk, M. Flieger, I. V. Maznichenko, I. Mertig, A. Ernst, S. V. Ereemeev, and E. V. Chulkov, *Phys. Rev. Lett.* **109**, 076801 (2012).
- ¹¹ L. B. Abdalla, L. Seixas, T. M. Schmidt, R. H. Miwa, and A. Fazzio, *Phys. Rev. B* **88**, 045312 (2013).
- ¹² Y. Li, X. Zou, J. Li, and G. Zhou, *The Journal of Chemical Physics* **140**, 124704 (2014).
- ¹³ Y. L. Chen, J.-H. Chu, J. G. Analytis, Z. K. Liu, K. Igarashi, H.-H. Kuo, X. L. Qi, S. K. Mo, R. G. Moore, D. H. Lu, M. Hashimoto, T. Sasagawa, S. C. Zhang, I. R. Fisher, Z. Hussain, and Z. X. Shen, *Science* **329**, 659 (2010).
- ¹⁴ M. R. Scholz, J. Sánchez-Barriga, D. Marchenko, A. Varykhalov, A. Volykhov, L. V. Yashina, and O. Rader, *Phys. Rev. Lett.* **108**, 256810 (2012).
- ¹⁵ T. Valla, Z.-H. Pan, D. Gardner, Y. S. Lee, and S. Chu, *Phys. Rev. Lett.* **108**, 117601 (2012).
- ¹⁶ J. Honolka, A. A. Khajetoorians, V. Sessi, T. O. Wehling, S. Stepanow, J.-L. Mi, B. B. Iversen, T. Schlenk, J. Wiebe, N. B. Brookes, A. I. Lichtenstein, P. Hofmann, K. Kern, and R. Wiesendanger, *Phys. Rev. Lett.* **108**, 256811 (2012).
- ¹⁷ T. M. Schmidt, R. H. Miwa, and A. Fazzio, *Journal of Physics: Condensed Matter* **25**, 445003 (2013).
- ¹⁸ L. A. Wray, S.-Y. Xu, Y. Xia, D. Hsieh, A. V. Fedorov, Y. San Hor, R. J. Cava, A. Bansil, H. Lin, and M. Z. Hasan, *Nature Physics* **7**, 32 (2011).
- ¹⁹ Y. S. Hor, P. Roushan, H. Beidenkopf, J. Seo, D. Qu, J. G. Checkelsky, L. A. Wray, D. Hsieh, Y. Xia, S.-Y. Xu, D. Qian, M. Z. Hasan, N. P. Ong, A. Yazdani, and R. J. Cava, *Phys. Rev. B* **81**, 195203 (2010).
- ²⁰ S.-Y. Xu, M. Neupane, C. Liu, D. Zhang, A. Richardella, L. A. Wray, N. Alidoust, M. Leandersson, T. Balasubramanian, J. Sánchez-Barriga, *et al.*, *Nature Physics* **8**, 616 (2012).
- ²¹ L. R. Shelford, T. Hesjedal, L. Collins-McIntyre, S. S. Dhesi, F. Maccherozzi, and G. van der Laan, *Phys. Rev. B* **86**, 081304 (2012).
- ²² Z. L. Li, J. H. Yang, G. H. Chen, M.-H. Whangbo, H. J. Xiang, and X. G. Gong, *Phys. Rev. B* **85**, 054426 (2012).
- ²³ J.-M. Zhang, W. Zhu, Y. Zhang, D. Xiao, and Y. Yao, *Phys. Rev. Lett.* **109**, 266405 (2012).
- ²⁴ J. Henk, A. Ernst, S. V. Ereemeev, E. V. Chulkov, I. V. Maznichenko, and I. Mertig, *Phys. Rev. Lett.* **108**, 206801 (2012).

- ²⁵ T. M. Schmidt, R. H. Miwa, and A. Fazio, Phys. Rev. B **84**, 245418 (2011).
- ²⁶ R. R. Biswas and A. V. Balatsky, Phys. Rev. B **81**, 233405 (2010).
- ²⁷ D. A. Abanin and D. A. Pesin, Phys. Rev. Lett. **106**, 136802 (2011).
- ²⁸ D. K. Efimkin and V. Galitski, Phys. Rev. B **89**, 115431 (2014).
- ²⁹ Y. H. Choi, N. H. Jo, K. J. Lee, H. W. Lee, Y. H. Jo, J. Kajino, T. Takabatake, K.-T. Ko, J.-H. Park, and M. H. Jung, Appl. Phys. Lett. **25**, 206005 (2013).
- ³⁰ P. Janíček, Č. Drašar, P. Lošták, J. Vejpravová, and V. Sechovský, Physica B: Condensed Matter **403**, 3553 (2008).
- ³¹ M. R. Mahani, M. F. Islam, A. Pertsova, and C. M. Canali, Phys. Rev. B **89**, 165408 (2014).
- ³² V. I. Anisimov, J. Zaanen, and O. K. Andersen, Phys. Rev. B **44**, 943 (1991).
- ³³ P. Blaha, K. Schwarz, G. K. H. Madsen, D. Kvasnicka, and J. Luitz, *WIEN2k, An Augmented Plane Wave Plus Local Orbitals Program for Calculating Crystal properties (Vienna University of Technology, Austria)* (2001).
- ³⁴ J. P. Perdew, K. Burke, and M. Ernzerhof, Phys. Rev. Lett. **77**, 3865 (1996).
- ³⁵ K. Kobayashi, Phys. Rev. B **84**, 205424 (2011).
- ³⁶ A. Pertsova and C. Canali, New J. Phys **16**, 063022 (2014).
- ³⁷ B. C. Chapler, K. W. Post, A. R. Richardella, J. S. Lee, J. Tao, N. Samarth, and D. N. Basov, Phys. Rev. B **89**, 235308 (2014).